Sulym et al. Nanoscale Research Letters (2016) 11:111
DOI 10.1186/s11671-016-1304-1

Nanoscale Research Letters
a SpringerOpen Journal

NANO COMMENTARY Open Access

Silica-Supported Titania–Zirconia Nanocomposites: Structural and Morphological Characteristics in Different Media

Iryna Sulym[1], Olena Goncharuk[1*], Dariusz Sternik[2], Ewa Skwarek[2], Anna Derylo-Marczewska[2], Wladyslaw Janusz[2] and Vladimir M. Gun'ko[1]

Abstract

A series of TiO_2–ZrO_2/SiO_2 nanocomposites were synthesized using a liquid-phase method and characterized by various techniques, namely, nitrogen adsorption–desorption, X-ray diffraction (XRD), X-ray photoelectron spectroscopy (XPS), Raman spectroscopy, high-resolution transmission electron microscopy, and photon correlation spectroscopy (PCS). It was revealed that the component ratio and calcination temperature affect the phase composition of nanocomposites. Composites TiZrSi1 (TiO_2:ZrO_2:SiO_2 = 3:10:87) and TiZrSi2 (10:10:80) calcined at 1100 °C demonstrate the presence of *t*-ZrO_2 crystallites in TiZrSi1 and $ZrTiO_4$ phase in TiZrSi2. The samples calcined at 550 °C were amorphous as it was found from XRD data. According to the Raman spectra, the bands specific for anatase are observed in TiZrSi2. According to XPS data, Zr and Ti are in the highest oxidation state (+4). Textural analysis shows that initial silica is mainly meso/macroporous, but composites are mainly macroporous. The particle size distributions in aqueous media showed a tendency of increasing particle size with increasing TiO_2 content in the composites.

Keywords: Nanocomposites, TiO_2–ZrO_2/SiO_2, Phase composition, Nanocrystallinity, Particle size distribution

Background

Highly disperse (nanoparticulate) oxide composites are of great interest for individual applications not only as heterogeneous catalysts with an adjustable set and strength of surface active sites [1–4] but also as a part of organic–inorganic composites and polymer fillers [5, 6]. Combination of dissimilar oxides allows to create surface active sites, which are absent in individual components [7]. The nature of active sites of solid acid catalysts is defined by mobile surface protons generating Brønsted acid sites and coordinately unsaturated cationic centers as Lewis acid sites [8]. Therefore, much attention has been focused on development of binary or ternary metal oxides as heterogeneous catalysts [1]. Thus, the main objective to prepare such nanoscale systems is aimed at controlling their surface composition and particle morphology. One of the common methods of the synthesis of nanoparticulate oxides is based on the use of a substrate of a high specific surface area. The fumed silica properties are a convenient vehicle for the synthesis of the mentioned composites due to silica inertness in catalytic processes, developed surface area, and homogeneity of active sites on a surface [9]. Among various metal oxide catalysts, the combination of titania and zirconia has attracted attention in recent years. These mixed oxides have been extensively used as catalysts and catalyst supports for a wide variety of reactions [2]. TiO_2–ZrO_2 mixed oxide composites are used as photocatalysts due to a reduced bandgap in comparison to individual components [3, 10–15]. They have been reported to exhibit a high surface acidity due to an imbalance of charges resulting from the formation of the Ti–O–Zr bridges [14, 16]. According to [11], TiO_2/SiO_2 and TiO_2/ZrO_2 are characterized by more acidic properties than single/pure components. TiO_2–ZrO_2 system is a strong solid acid showing catalytic activity in such reactions as isomerization and cracking of alkanes, hydration

* Correspondence: iscgoncharuk@meta.ua
[1]Chuiko Institute of Surface Chemistry, NASU, 17 General Naumov Str., 03164 Kyiv, Ukraine
Full list of author information is available at the end of the article

and polymerization of alkenes, etc. [7, 17]. The most widely employed methods to prepare TiO_2–ZrO_2 composites are co-precipitation [18, 19] and sol–gel synthesis [2, 10, 20, 21]. A method of grafting of mixed oxides onto a surface of highly disperse matrices with nonporous nanoparticles can be a good alternative to the mentioned methods. Therefore, the objective of this study was the synthesis of silica-supported titania–zirconia nanocomposites (TiO_2–ZrO_2/SiO_2) and investigation of their morphological and structural properties.

Methods

Materials

Fumed silica (pilot plant of the Chuiko Institute of Surface Chemistry, Kalush, Ukraine), zirconium (Aldrich, > 98 % $Zr(acac)_4$), and titanyl ($C_{10}H_{11}O_5Ti$) acetylacetonates (Merck) were used as precursors to prepare oxide composites.

Synthesis of Silica-Supported Titania–Zirconia Nanocomposites

Silica-supported titania–zirconia nanocomposites (TiO_2–ZrO_2/SiO_2) were prepared using a liquid-phase method. The synthesis was performed in a glass double-neck reactor equipped with a propeller agitator and a reflux condenser. $Zr(acac)_4$ and $C_{10}H_{11}O_5Ti$ solutions in isopropyl alcohol (IPA) were added to fumed silica (5 g; previously calcined at 500 °C; specific surface area $S = 283$ m^2/g) at 82.5 °C. The reaction mixture was stirred in the refluxing tube for 1 h. Then, IPA and acetylacetone were removed from the mixture by evacuation. The solid products were dried and calcined at 550 °C and 1100 °C for 1 h. According to [22], the temperature range 500–550 °C corresponds to the destruction of acetylacetonate ligands and complete removal of the volatile carbon components upon oxide formation. But at 550 °C, a high probability of the formation of the amorphous structure takes place, while the temperature of 1100 °C was chosen as sufficient for crystalline structure formation. The content of grafted TiO_2 was varied from 3 to 10 wt.% while ZrO_2 content was held constant at 10 wt.% (samples TiZrSi1 and TiZrSi2, respectively).

X-Ray Powder Diffraction Analysis (XRD)

X-ray diffraction patterns were recorded at room temperature using a DRON-3M diffractometer (Burevestnik, St. Petersburg, Russia) with Cu K_α ($\lambda = 0.15418$ nm) radiation and a Ni filter in the 2θ range from 10° to 70°. The average size of nanocrystallites (D_{cr}) was estimated according to the Scherrer equation [23]. Crystalline structure of samples was analyzed using the JCPDS Database (International Center for Diffraction Data, PA, 2001) [24]. Silica was totally amorphous in all samples.

Raman Spectroscopy (RS)

The Raman spectra were recorded over the 150–3200-cm^{-1} range using an inVia Reflex Microscope DMLM Leica Research Grade, Reflex (Renishaw, UK), with Ar^+ ion laser excitation at $\lambda_0 = 514.5$ nm. For each sample, the spectra were recorded at several points in order to ascertain the homogeneity of the sample, and the averages of all these spectra were plotted.

X-Ray Photoelectron Spectroscopy (XPS)

The XPS measurements were performed using a VG Scienta R4000 electron analyzer with an MX650 monochromatized Al K_α (1486.6 eV) radiation source. The binding energy (BE) was referenced to Si 2p (BE = 103.5 eV) with an accuracy of ±0.1 eV. Peak fitting was done using Casa XP5 with Shirley background and 10:90 Lorentzian/Gaussian convolution product shapes. The atomic concentration ratios were achieved by determining the elemental peak areas, following a Shirley background subtraction by the usual procedures documented in the literature [25].

High-Resolution Transmission Electron Microscopy (HRTEM)

The particulate morphology was analyzed using high-resolution transmission electron microscope (HRTEM) employing a Tecna™ G2 T20 X-TWIN (FEI Company, USA) apparatus operating at a voltage of 200 kV with LaB6 electron source. The samples were supported on holey carbon copper grids by dropping ethanol suspensions containing uniformly dispersed oxide powders.

Textural Characterization

To analyze the textural characteristics of TiO_2–ZrO_2/SiO_2 nanocomposites, low-temperature (77.4 K) nitrogen adsorption–desorption isotherms were recorded using an automatic gas adsorption analyzer ASAP 2405N (Micromeritics Instrument Corp., USA) after outgassing the samples at 110 °C for 2 h in a vacuum chamber. The values of the specific surface area (S_{BET}) were calculated according to the standard BET method [26]. The total pore volume V_p was evaluated by converting the volume of adsorbed nitrogen at $p/p_0 = 0.98$–0.99 (p and p_0 denote the equilibrium pressure and saturation pressures of nitrogen at 77.4 K, respectively) to the volume of liquid nitrogen per gram of adsorbent. The nitrogen desorption data were used to compute the pore size distributions (differential $f_V \sim dV_p/dR$ and $f_S \sim dS/dR$) using a self-consistent regularization (SCR) procedure under non-negativity condition ($f_V \geq 0$ at any pore radius R) at a fixed regularization parameter $\alpha = 0.01$ with voids (V) between spherical nonporous nanoparticles packed in random aggregates (V/SCR model) [27]. The differential pore size distributions with respect to pore volume $f_V \sim dV/dR$, $\int f_V dR \sim V_p$ were re-calculated to incremental pore

size distributions (IPSD) at $\Phi_V(R_i) = (f_V(R_{i+1}) + f_V(R_i))(R_{i+1} - R_i)/2$ at $\Sigma\Phi_V(R_i) = V_p$). The f_V and f_S functions were also used to calculate contributions of micropores (V_{micro} and S_{micro} at 0.35 nm < R < 1 nm), mesopores (V_{meso} and S_{meso} at 1 nm < R < 25 nm), and macropores (V_{macro} and S_{macro} at 25 nm < R < 100 nm).

Particle Size Distribution in Aqueous Media

Particle sizing for the aqueous suspensions of different fine oxides were carried out using a Zetasizer 3000 (Malvern Instruments) apparatus based on photon correlation spectroscopy (PCS, $\lambda = 633$ nm, $\Theta = 90°$, software version 1.3).

The aqueous suspensions of oxides 0.1 wt.% were prepared using an ultrasonic disperser for 5 min (Sonicator Misonix Inc., power 500 W and frequency 22 kHz) prior to measuring particle size distribution.

Discussion

Textural Characterization

The nitrogen adsorption–desorption isotherms obtained for initial silica and composites (Fig. 1a) demonstrate sigmoidal-shaped behavior with a narrow hysteresis loop. The incremental pore (voids between particles in aggregates) size distribution functions (Fig. 1b) show that the textural characteristics change after the modification.

The specific surface area (Table 1, S_{BET}) does not demonstrate a significant reduction after grafting of titania/zirconia. However, the total pore volume increases for TiO_2–ZrO_2/SiO_2 compared to the initial silica. Furthermore, there is a significant decrease in mesopore contribution to the total porosity with a simultaneous increase in contribution of macropores. Moreover, the microporosity is slightly reduced for composites compared to the initial silica. Thus, the analysis of the results suggests the existence of mainly meso/macroporosity of aggregates of the initial silica and mainly macroporosity of the composites (Fig. 1b).

High-Resolution Transmission Electron Microscopy

HRTEM images of TiO_2–ZrO_2/SiO_2 nanocomposites (Fig. 2) show the formation of titania–zirconia particles (dark structures) at the silica surface (light structures). The aggregated structures of grafted oxides varying between 15 and 50 nm in size are well observed for TiZrSi1–2. Composites look like more compacted than initial silica. Therefore, contribution of macropores increases (Fig. 1b), as well as the total pore volume V_p and V_{macro} (Table 1) as an increased part of the empty volume ($V_{em} = 1/\rho_b - 1/\rho_0$, where ρ_0 and ρ_b are the true density of oxide nanoparticles and bulk density of the powder, respectively), in the powders. Note that any treatment or modification of fumed silica results in a decrease in the value of V_{em}, i.e., the value of ρ_b increases, and sometimes the value of V_p increases, despite a decrease in V_{em}, because nitrogen can fill only a portion of macropores even at $p/p_0 \to 1$ [28].

X-Ray Powder Diffraction Analysis

XRD analysis of TiO_2–ZrO_2/SiO_2 containing different amounts of TiO_2 (Fig. 3) shows that the samples TiZrSi1 and TiZrSi2 calcined at 550 °C are amorphous. A broad peak in the range of 20–23° is due to amorphous silica [29, 30]. Calcination at 1100 °C resulted in the appearance of crystalline phases: t-ZrO_2 (PDF-ICDD 80-0965) for TiZrSi1 and $ZrTiO_4$ (PDF-ICDD 74-1504) for TiZrSi2 (Table 2). For TiZrSi1, there are four sharp peaks at 30.5°, 35.3°, 50.4°, and 60.2°, which can be attributed to diffraction planes (111), (200), (220), and (311) of tetragonal zirconia (No. 79–1771). TiZrSi2 is characterized by peaks at 25.3°, 30.5°, 35.3°, 42.1°, 50.4°, 53.8°, and 61.4°, which can be assigned to the planes (101), (111), (200), (211), (202), (204), and (311) of crystalline $ZrTiO_4$. The broad diffraction peaks indicated a small size of crystallites that signifies the influence of the silica substrate preventing consolidation of nuclei of grafted oxides. The average size of crystallites (D_{cr}) revealed a nominal increase with increasing titania content (Table 2). Thus, the use

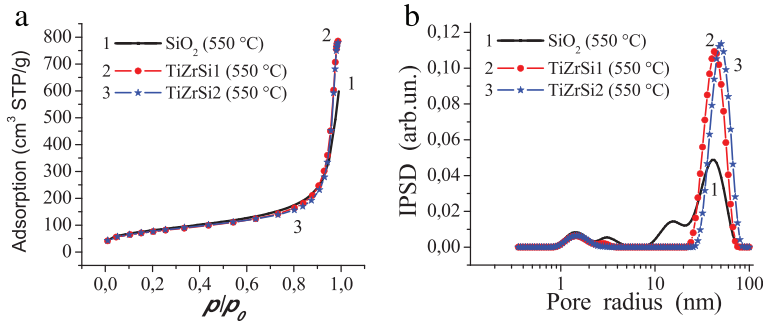

Fig. 1 Nitrogen adsorption–desorption isotherms (**a**) and incremental pore size distributions (**b**) for initial silica (*curve 1*), TiZrSi1 (*2*), and TiZrSi2 (*3*) calcined at 550 °C

Table 1 Textural characteristics of initial and titania–zirconia-coated silica

Sample	S_{BET} (m^2/g)	S_{micro} (m^2/g)	S_{meso} (m^2/g)	S_{macro} (m^2/g)	V_{micro} (cm^3/g)	V_{meso} (cm^3/g)	V_{macro} (cm^3/g)	V_p (cm^3/g)	$R_{p,V}$ (nm)
SiO_2	283	21	225	38	0.008	0.35	0.57	0.93	29
TiZrSi1	276	17	163	97	0.005	0.08	1.12	1.21	39
TiZrSi2	280	18	169	92	0.005	0.07	1.13	1.20	45

Specific surface area in total (S_{BET}), of nanopores (S_{micro}), mesopores (S_{meso}), macropores (S_{macro}), and respective specific pore volumes (V_p, V_{micro}, V_{meso}, V_{macro}). $R_{p,V}$ represents the average pore radius determined from the differential pore size distributions with respect to the pore volume

of fumed silica as the inert substrate results in the formation of small nanocrystallites of grafted oxides, only.

Raman Spectroscopy

Raman spectroscopy (Fig. 4) allows to get more information on the sample structure, composition effects, features of phase transition, and the quantum size effect. Fumed silica does not show any Raman features, as reported in the literature [31, 32]. It is known that zirconia exists as three polymorphs: monoclinic (*m*-ZrO_2), tetragonal (*t*-ZrO_2), and cubic (*c*-ZrO_2). However, no Raman bands at 280, 316, 462, and 644 cm^{-1} due to tetragonal ZrO_2 [33] or at 615 and 638 cm^{-1} due to monoclinic ZrO_2 [34] are observed.

Additionally, no Raman bands at 148, 263, 476, and 550 cm^{-1} due to three-dimensional amorphous zirconia [35] are detected. For each sample, the spectra were recorded at several points, and no shift in the band position or differences of width were observed. This observation clearly reveals that all of the samples are mostly in a homogeneous state. For sample TiZrSi1, characteristic Raman bands are not observed. However, for sample TiZrSi2, the well-resolved Raman peaks at 143, 400, 500, 518, 630, 810, and 1083 cm^{-1} are observed. Some of these bands are specific to anatase [36] at 143 cm^{-1} (E_g, very strong), 197 cm^{-1} (E_g), 396 cm^{-1} (B_{1g}), 514 cm^{-1} (A_{1g}, B_{1g}), and 637 cm^{-1} (E_g).

The obtained Raman spectrum is well correlated with the data for $ZrTiO_4$ [37, 38]. It was noted [33] that the

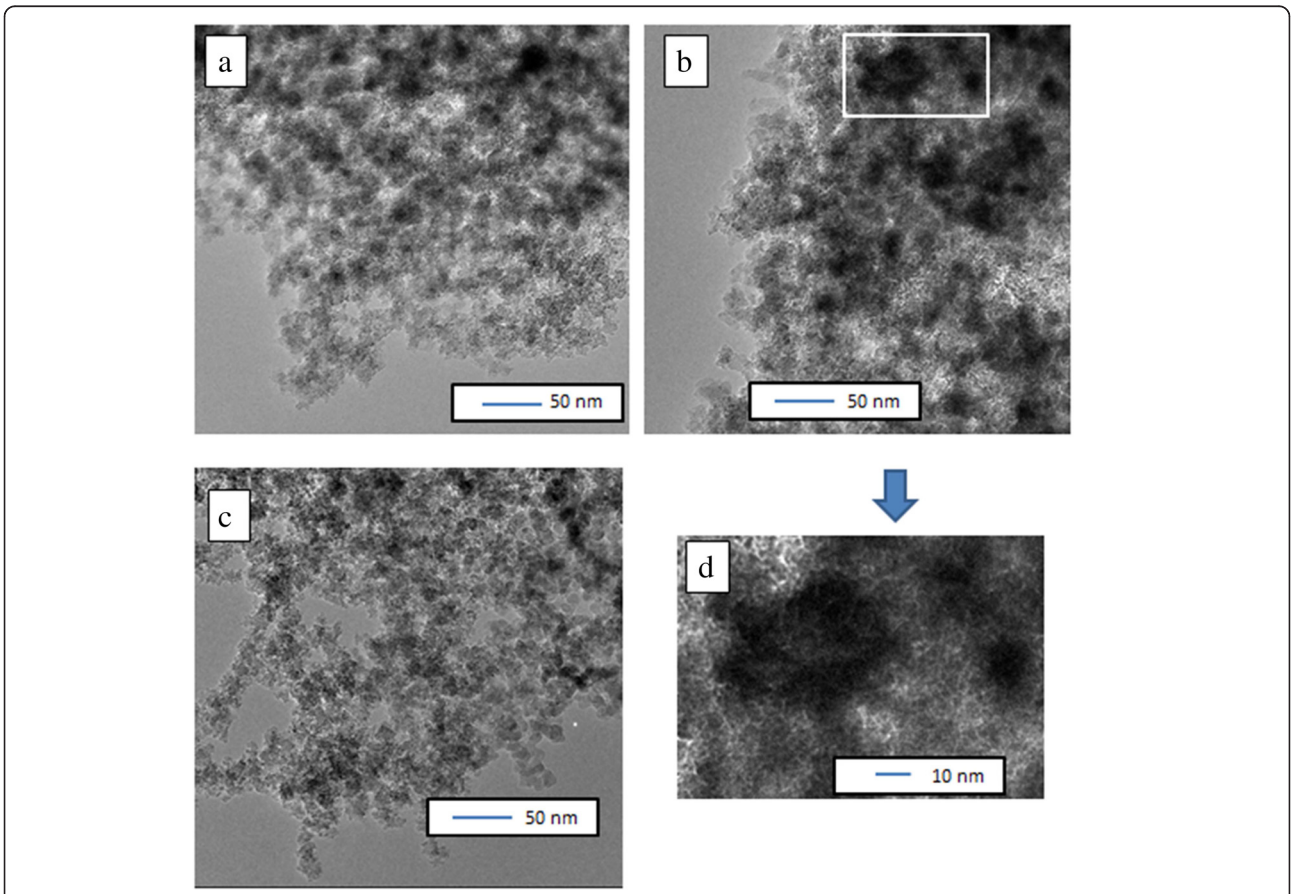

Fig. 2 TEM micrographs of TiZrSi1 (**a**) and TiZrSi2 (**b**, **d**) samples calcined at 550 °C and initial SiO_2 (**c**)

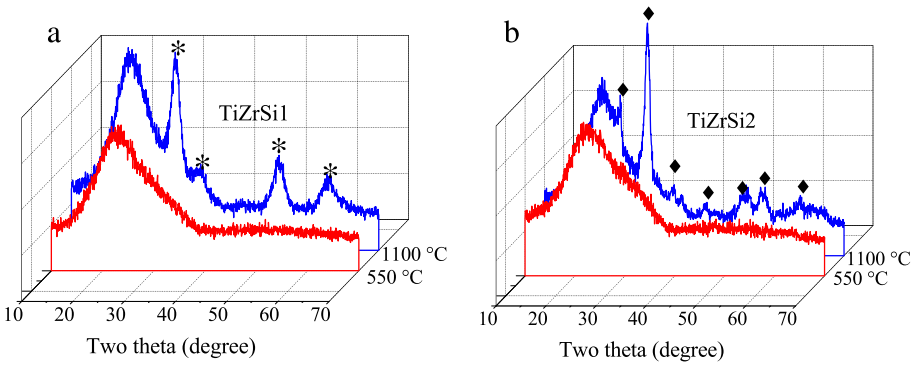

Fig. 3 XRD patterns of TiZrSi1 (**a**) and TiZrSi2 (**b**) samples calcined at 550 and 1100 °C. *Asterisks* correspond to *t*-ZrO_2 and *black diamonds* correspond to $ZrTiO_4$

variations in broad bands at 148 (E_g), 401 (B_{1g}), 522 (A_{1g} or B_{1g}), and 648 (E_g) cm^{-1} are characteristic for anatase depending on the ratio TiO_2:ZrO_2 in films, but no other bands characteristic for other polymorphs were found. According to [37], the degree of line broadening in a peak at 815 cm^{-1} as probing local microstructure was chosen because this peak did not overlap with other peaks and exhibited a pronounced change in the degree of line broadening.

Thus, it can be seen that anatase is formed only at relatively high concentration of TiO_2 in the composite, whereas at a low concentration of TiO_2, the amorphous titania is observed. Based on the presence of the background at the location of line $E_g(1)$ for TiZrSi2, an amorphous phase is also present. The intensity of the Raman bands depends on several factors including grain size and morphology [38]. A strong increase in line $E_g(1)$ background at the presence of small (2–3 nm) crystallites was also noted previously [39]. Peak $E_g(2)$ near 197 cm^{-1} has a very low intensity and in our composites is not observed.

The absence of any other Raman features providing inference that silica does not form any compound with titania and zirconia is in line with XRD observations.

Surface Characterization by XPS

Formation of chemical bonds between components in ternary oxides was investigated using the XPS method (Fig. 5). Two main peaks for silicon (Si 2s and Si 2p), two peaks for zirconium (Zr 3p and Zr 3d), and only one main peak for titanium (Ti 2p doublet) were detected in the spectra (Fig. 5). For all the samples, analysis of the 1s line of the carbon showed that the states with a binding energy within 284.7–290.8 eV are formed by a

Table 2 Characteristics of TiO_2–ZrO_2/SiO_2 composites calcined at different temperatures

Sample ID	Composition	C_{ZrO2} (wt.%)	C_{TiO2} (wt.%)	C_{SiO2} (wt.%)	D_{cr} (nm)	
					550 °C	1100 °C
SiO_2	SiO_2	–	–	100		a
TiZrSi1	TiO_2–ZrO_2/SiO_2	10	3	87	a	4 (b)
TiZrS2	TiO_2–ZrO_2/SiO_2	10	10	80	a	7 (c)

a amorphous, *b* *t*-ZrO_2, *c* $ZrTiO_4$

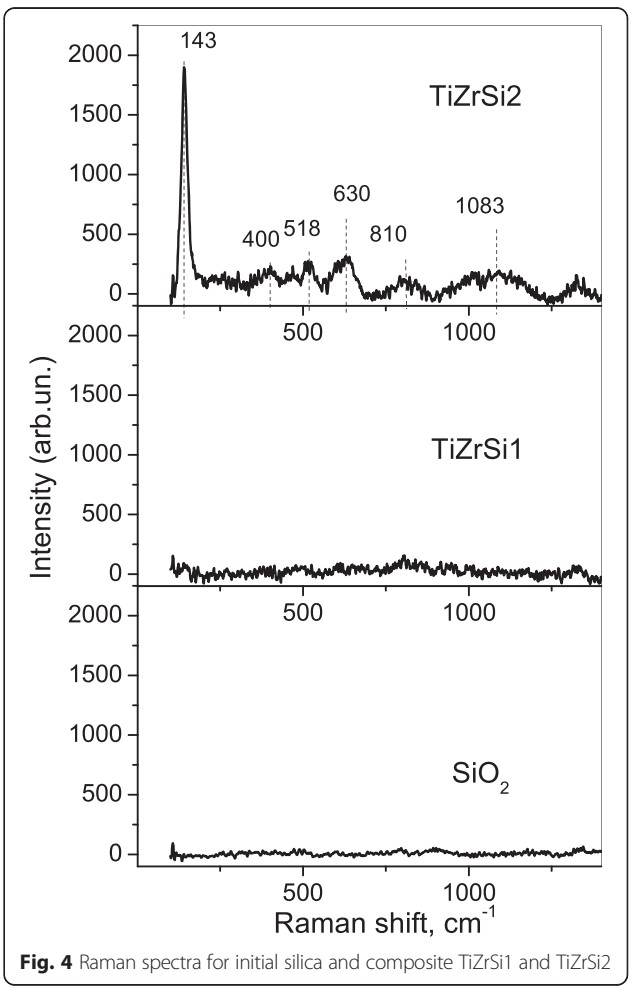

Fig. 4 Raman spectra for initial silica and composite TiZrSi1 and TiZrSi2

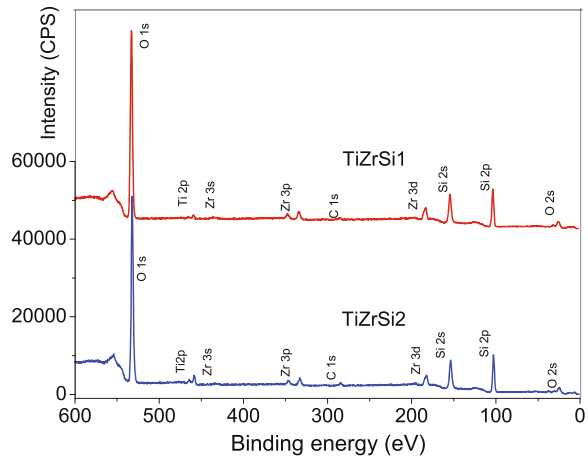

Fig. 5 Wide XPS spectra: TiZrSi1 and TiZrSi2

variety of carbon bonds of surface hydrocarbon contamination of samples [40].

For the analysis of the chemical state of elements forming nanolayers TiO_2–ZrO_2/SiO_2, the following line core levels Si 2p, O 1s, Zr 3d, and Ti 2p were selected. The detailed XPS spectra of oxygen for silica and ternary oxide samples are compared (Fig. 6a). In oxygen O 1s region, one can see that the positions of O 1s are slightly shifted in samples TiZrSi1 and TiZrSi1 compared to the initial silica. For TiO_2–ZrO_2/SiO_2, the O 1s peak can be divided into two bands O 1s A and O 1s B, and the ratio of these components depends on the content of titania (Fig. 6 and Table 3). The appearance of the O 1s peak at lower energy is due to the effects of TiO_2 and ZrO_2 with a large displacement of the electron density to the O atoms than that in silica.

The binding energy of the Si 2p peak ranged between 103.5 and 103.7 eV (Fig. 6b) that are consistent with the values reported in the literature [40]. The weak intensity

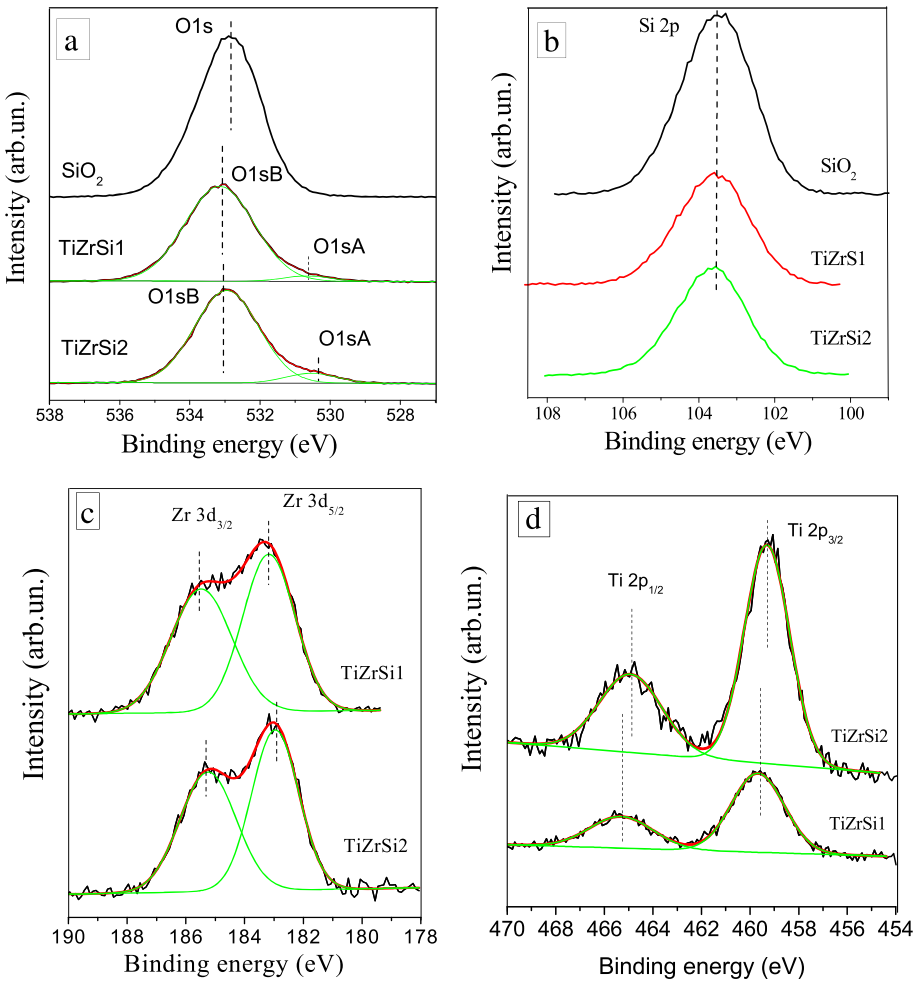

Fig. 6 Detailed XPS of O 1s (**a**), Si 2p (**b**), Zr 3d (**c**), and Ti 2p (**d**) initial silica (Si 2p, O 1s) and TiO_2–ZrO_2/SiO_2 at different contents of TiO_2 (TiZrSi1 and TiZrSi2) calcined at 550 °C

Table 3 XPS core-level binding energy values (eV) for samples studied

Sample ID	O 1s	Si 2p	Zr $3d_{5/2}$	Zr $3d_{3/2}$	Ti $2p_{3/2}$	Ti $2p_{1/2}$
SiO_2	532.90	103.52	–	–	–	–
TiZrSi1	530.5	103.6	183.3	185.6	459.6	465.4
	533.2					
TiZrSi2	530.5	103.7	183.1	185.4	459.3	465.0
	533.0					

of the spectra with large peak widths in case of TiZrSi1 and TiZrSi1 samples indicates that silica is not easily accessible at the surface due to the presence of titania–zirconia layers.

The Zr $3d_{5/2}$ and Ti $2p_{3/2}$ peaks (Fig. 6c, d) correspond to the binding energy of 183.1–183.3 and 459.3–459.6 eV, respectively, which represent the fully oxidized zirconium ion Zr^{4+} and titanium ion Ti^{4+} [39]. Such binding energies can be attributed both to the individual metal oxides [39] and to $ZrTiO_4$ [41, 42]. The observed positive shifts of the peaks Ti $2p_{3/2}$ and Ti $2p_{1/2}$ (Fig. 6d) relatively to the peaks in individual titania (458.7 and 464.7 eV) [40] may testify the formation of the Ti–O–Zr bonds. The displacement was observed [43] for the mixed triple films $TiO_2/ZrO_2/SiO_2$. Note that during mixed oxide formation, the inhibitive influence on the growth and agglomeration of the individual phases of the components occurs due to the formation of the Ti–O–Zr bonds. In the investigated samples, the shift of the Ti $2p_{3/2}$ peak relatively to pure TiO_2 is larger for TiZrSi1 at smaller content of TiO_2 than for TiZrSi2 with a high content of TiO_2. This fact shows that at increasing TiO_2 content in the ternary oxide, the number of the Ti–O–Zr bonds decreases, i.e., at higher content, TiO_2 forms a separate phase, while at lower content it forms TiO_2–ZrO_2 mixed oxide.

Particle Size Distribution

The degree of aggregation/agglomeration of nanoparticles depends on their characteristics and interactions with the dispersion medium. The initial silica is characterized by nearly monomodal particle size distribution (PSD) with a maximum at 21 nm (Fig. 7a, curve 1).

However, the PSD for composites is bimodal with two peaks with respect to the particle number (Fig. 7a) and particle volume (Fig. 7b). The PSDs for TiZrSi1 and initial silica are similar, while for TiZrSi2, the aggregates are characterized by larger sizes ~500 nm. Note that there is a tendency of increasing particle size with increasing TiO_2 content in the composites (Fig. 7, curves 2–3). The increase of the average particle size in aqueous suspensions can be associated as with a change in particle size during the formation of a new phase of ZrO_2/TiO_2 during the synthesis and also with influence of changes in surface structure and related electrokinetic properties of the oxide composites on the aggregation processes in an aqueous medium.

Conclusion

In the present study, highly disperse silica-supported titania–zirconia nanocomposites were synthesized by a liquid-phase method. The samples were examined using a set of techniques after their calcination at 550 and 1100 °C. The structural characteristics (phase composition, average size of crystallites) of the materials affected by pre-heating were determined from the XRD data. The XRD measurements indicated the presence of $ZrTiO_4$ and anatase in TiZrSi2 and tetragonal zirconia in TiZrSi1 calcined at 1100 °C. The TiZrSi1 and TiZrSi2 samples calcined at 550 °C were XRD amorphous. The crystallinity slightly increased with increasing titania content in nanocomposites. There is no indication of compound formed with silica and titania or zirconia. The analysis of

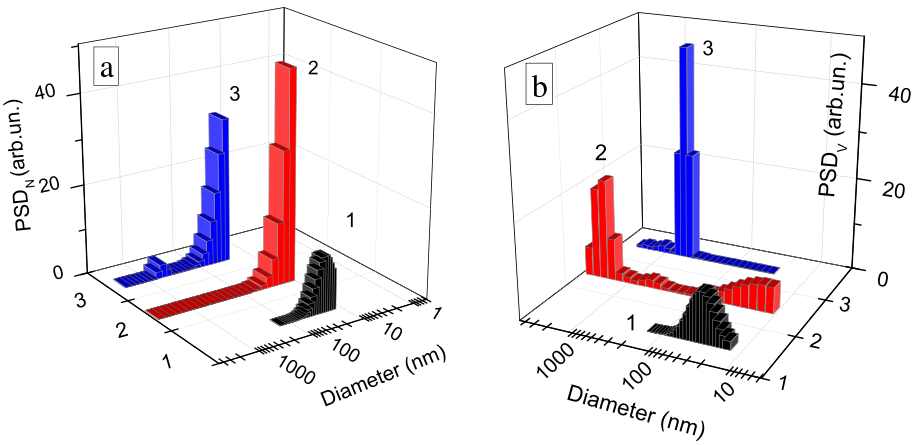

Fig. 7 PSD related to **a** particle number and **b** volume for silica and composites after sonication (3 min) of the aqueous suspensions ($C = 0.1$ wt.%) of initial SiO_2 (*1*), TiZrSi1 (*2*), and TiZrSi2 (*3*)

the nitrogen adsorption–desorption data and HRTEM indicates that the grafting new oxide phases changes the textural characteristics of the powders. The incremental pore size distribution functions revealed the existence of mainly meso/macroporosity of aggregates of initial silica and mainly macroporosity of TiO_2–ZrO_2/SiO_2 nanocomposites. The HRTEM images show the presence of well-dispersed Zr–Ti–oxide nanocrystallites ~15–50 nm in size on the amorphous silica matrix. In line with XRD results, Raman spectra show that silica did not form any compound with titania or zirconia. The XPS results reveal that O 1s, Si 2p, Zr 3d, and Ti 2p core-level photoelectron peaks are sensitive to the phase composition of TiO_2–ZrO_2/SiO_2 nanocomposites. Moreover, XPS measurements show that Zr and Ti ions are present in their highest oxidation states (+4). The shift of the peaks indicates the possible formation of titanium–zirconium mixed oxide. A tendency of increasing particle size with increasing TiO_2 content in the composites was detected accordingly to the PSD characterization in the aqueous media.

Competing Interests
The authors declare that they have no competing interests.

Authors' Contributions
IS carried out the synthesis and characterization of nanocomposites by XRD method. DS and ADM participated in the XPS, Raman, and TEM-HRTEM studies. ES, OG, and WJ participated in the measurement of PSD for nanocomposites. OG and IS analyzed the data and drafted the manuscript. VG and WJ designed the whole work and revised the manuscript. All authors read and approved the final manuscript.

Acknowledgements
The authors are grateful to the European Community, Seventh Framework Programme (FP7/2007–2013), Marie Curie International Research Staff Exchange Scheme (IRSES grant no. 612484), for the financial support of this work. The research was partly carried out with the equipment purchased thanks to the financial support of the European Regional Development Fund in the framework of the Polish Innovation Economy Operational Program (contract no. POIG.02.01.00-06-024/09 Center of Functional Nanomaterials).

Author details
[1]Chuiko Institute of Surface Chemistry, NASU, 17 General Naumov Str., 03164 Kyiv, Ukraine. [2]Faculty of Chemistry, Maria Curie-Sklodowska University, 20-031 Lublin, Poland.

Received: 26 November 2015 Accepted: 8 February 2016
Published online: 29 February 2016

References
1. Tanaka H, Boulinguiez M, Vrinat M (1996) Hydrodesulfurization of thiophene, dibenzothiophene and gas oil on various Co-Mo/TiO_2-Al_2O_3 catalysts. Catal Today 29:209–213
2. Manríquez ME, López T, Gómez R, Navarrete J (2004) Preparation of TiO_2–ZrO_2 mixed oxides with controlled acid–basic properties. J Mol Catal A-Chem 220(2):229–237
3. Reddy BM, Khan A (2005) Recent advances on TiO_2-ZrO_2 mixed oxides as catalysts and catalyst supports. Catalysis Rev 47:257–296
4. Vishwanathan V, Roh HS, Kim JW, Jun KW (2004) Surface properties and catalytic activity of TiO_2–ZrO_2 mixed oxides in dehydration of methanol to dimethyl ether. Catal Lett 96:23–28
5. Lü C, Yang B (2009) High refractive index organic–inorganic nanocomposites: design, synthesis and application. J Mater Chem 19:2884–2901
6. Hanemann T, Szabó DV (2010) Polymer-nanoparticle composites: from synthesis to modern applications. Materials 3:3468–3517
7. Tanabe K, Misono M, Ono Y, Hattori H (1989) New solids and bases. Kodansha–Elsevier, Tokyo
8. Corma A (1995) Inorganic solid acids and their use in acid-catalyzed hydrocarbon reactions. Chem Rev 95(3):559–614. doi:10.1021/cr00035a006
9. Iler RK (1979) The chemistry of silica: solubility, polymerization, colloid and surface properties and biochemistry of silica. Wiley, New York
10. Tomar LJ, Chakrabarty BS (2013) Synthesis, structural and optical properties of TiO_2-ZrO_2 nanocomposite by hydrothermal method. Adv Mat Lett 4(1):64–67
11. Fu X, Clark LA, Yang Q, Anderson MA (1996) Enhanced photocatalytic performance of titania-based binary metal oxides: TiO_2/SiO_2 and TiO_2/ZrO_2. Environ Sci Technol 30:647–653
12. Navio JA, Hidalgo MC, Roncel M, De la Rosa MA (1999) A laser flash photolysis study of the photochemical activity of a synthesised $ZrTiO_4$. Comparison with parent oxides, TiO_2 and ZrO_2. Mater Lett 39(6):370–373
13. Kim JY, Kim CS, Chang HK, Kim TO (2010) Effects of ZrO_2 addition on phase stability and photocatalytic activity of ZrO_2/TiO_2 nanoparticles. Adv Powder Technol 21(2):141–144
14. Wu B, Yuan R, Fu X (2009) Structural characterization and photocatalytic activity of hollow binary ZrO_2/TiO_2 oxide fibers. J Solid State Chem 182(3): 560–565
15. Zhang M, Yu X, Lu D, Yang J (2013) Facile synthesis and enhanced visible light photocatalytic activity of N and Zr co-doped TiO_2 nanostructures from nanotubular titanic acid precursors. Nanoscale Res Lett 8:543
16. Reddy BM, Chowdhury B, Smirniotis PG (2001) An XPS study of the dispersion of MoO_3 on TiO_2–ZrO_2, TiO_2–SiO_2, TiO_2–Al_2O_3, SiO_2–ZrO_2, and SiO_2–TiO_2–ZrO_2 mixed oxides. Appl Catal A 211:19–30
17. Yamaguchi T (1990) Recent progress in solid superacid. Appl Catal 61:1–25
18. Koohestania H, Alinezhad M, Sadrnezhaad SK (2015) Characterization of TiO_2-ZrO_2 nanocomposite prepared by co-precipitation method. In: Advances in Nanocomposite Research., http://docs.sadrnezhaad.com/papers/564.pdf, accessed 15 Feb 2015
19. Lin W, Lin L, Zhu YX, Xie YC, Scheurell K, Kemnitz E (2005) Novel Pd/TiO_2–ZrO_2 catalysts for methane total oxidation at low temperature and their ^{18}O-isotope exchange behavior. J Mol Catal A-Chem 226(2):263–268
20. Perez-Hernandez R, Mendoza-Anaya D, Fernandez ME, Gomez-Cortes A (2008) Synthesis of mixed ZrO_2–TiO_2 oxides by sol–gel: microstructural characterization and infrared spectroscopy studies of NO_x. J Mol Catal A-Chem 281:200–206
21. Lakshmi JL, Ihasz NJ, Miller JM (2001) Synthesis, characterization and ethanol partial oxidation studies of V_2O_5 catalysts supported on TiO_2–SiO_2 and TiO_2–ZrO_2 sol–gel mixed oxides. J Mol Catal A-Chem 165(1–2):199–209
22. Borysenko MV, Sulim IY, Borysenko LI (2008) Modification of highly dispersed silica with zirconium acetylacetonate. Theor Exp Chem. doi:10.1007/s11237-008-9030-0
23. Jenkins R, Snyder RL (1996) Introduction to X-ray powder diffractometry. Wiley, New York
24. JCPDS Database, International Center for Diffraction Data, 2001. http://www.icdd.com.
25. Briggs D, Seah MP (eds) (1990) Auger and X-ray photoelectron spectroscopy. Practical surface analysis. Wiley, New York
26. Gregg SJ, Sing KSW (1982) Adsorption, surface area and porosity. Academic Press, London
27. Gun'ko VM (2014) Composite materials: textural characteristics. Appl Surf Sci 307:444–454
28. Gun'ko VM, Turov VV (2013) Nuclear magnetic resonance studies of interfacial phenomena. CRC Press, Boca Raton
29. Pengpeng L, Hailei Z, Jing W, Xin L, Tianhou Z, Qing X (2013) Facile preparation and electrochemical properties of amorphous SiO_2/C composite as anode material for lithium ion batteries. J Power Sources 237:291–294
30. Mao Z, Wu Q, Wang M, Yang Y, Long J, Chen X (2014) Tunable synthesis of SiO_2-encapsulated zero-valent iron nanoparticles for degradation of organic dyes. Nanoscale Res Lett 9:501
31. Reddy BM, Lakshmanan P, Khan A (2004) Investigation of surface structures of dispersed V_2O_5 on CeO_2-SiO_2, CeO_2-TiO_2, and CeO_2-ZrO_2 mixed oxides by XRD, Raman, and XPS techniques. J Phys Chem B 108:16855–16863
32. Reddy BM, Khan A (2005) Nanosized CeO_2–SiO_2, CeO_2–TiO_2, and CeO_2–ZrO_2 mixed oxides: influence of supporting oxide on thermal stability and oxygen storage properties of ceria. Catalysis Surv Asia 9:155–171
33. Gao X, Fierro JLG, Wachs IE (1999) Structural characteristics and catalytic properties of highly dispersed ZrO_2/SiO_2 and V_2O_5/ZrO_2/SiO_2 catalysts. Langmuir 1:3169–3178

34. Naumenko A, Gnatiuk Y, Smirnova N, Eremenko A (2012) Characterization of sol–gel derived TiO_2/ZrO_2 films and powders by Raman spectroscopy. Thin Solid Films 520:4541–4546
35. Picquart M, Lypez T, Gymez R, Torres E, Moreno A, Garcia J (2004) Dehydration and the crystallization process in sol-gel zirconia—thermal and spectroscopic study. J Therm Anal Calorim 76:755–761
36. Choi HC, Jung YM, Kim SB (2005) Size effects in the Raman spectra of TiO_2 nanoparticles. Vibrational Spectrosc 37(1):33–38
37. Kim YK, Jang HM (2003) Polarization leakage and asymmetric Raman line broadening in microwave dielectric $ZrTiO_4$. J Phys Chem Solids 64:1271–1278
38. Spanier JE, Robinson RD, Zhang F, Chan SW, Herman IP (2001) Size-dependent properties of CeO_2-y nanoparticles as studied by Raman scattering. Phys Rev B 64:245407-1–245407-8
39. Zhu KR, Zhang MS, Chen Q, Yin Z (2005) Size and phonon-confinement effects on low-frequency Raman mode of anatase TiO_2 nanocrystal. Phys Lett A 340(1–4):220–227
40. Wagner ChD, Naumkin AV, Kraut-Vass A, Allison JW, Powell CJ, Rumble JR (2012) NIST Standard Reference Database 20, Version 4.1. http://srdata.nist.gov/xps. Accessed 15 Sept 2012.
41. Ikawa H, Yamada T, Kojima K, Matsumoto S (1991) X-ray photoelectron spectroscopy study of high- and low-temperature forms of zirconium titanate. J Am Ceram Soc 74:1459–1462
42. Sham EL, Aranda MAG, Farfan-Torres EM, Gottifredi JC, Martı'nez-Lara M, Bruque S (1998) Zirconium titanate from sol–gel synthesis: thermal decomposition and quantitative phase analysis. J Solid State Chem 139:225
43. Andrulevičius M, Tamulevičius S, Gnatyuk Y, Vityuk N, Smirnova N, Eremenko A (2008) XPS investigation of $TiO_2/ZrO_2/SiO_2$ films modified with Ag/Au nanoparticles. Mat Sci (Medžiagotyra) 14(1):8, http://internet.ktu.lt/lt/mokslas/zurnalai/medz/pdf/medz0-92/02%20Electronic...(pp.08-14).pdf.